

# Mesonic spectroscopy of Minimal Walking Technicolor

Luigi Del Debbio,<sup>1,\*</sup> Biagio Lucini,<sup>2,†</sup> Agostino Patella,<sup>2,‡</sup> Claudio Pica,<sup>3,§</sup> and Antonio Rago<sup>4,¶</sup>

<sup>1</sup>*SUPA, School of Physics and Astronomy, University of Edinburgh, Edinburgh EH9 3JZ, Scotland*

<sup>2</sup>*School of Physical Sciences, Swansea University, Singleton Park, Swansea SA2 8PP, UK*

<sup>3</sup>*CP<sup>3</sup>-Origins, University of Southern Denmark, Odense, 5230 M, Denmark*

<sup>4</sup>*Department of Physics, Bergische Universität Wuppertal, Gausstr. 20, D-42119 Wuppertal, Germany*

(Dated: February 14, 2022)

We investigate the structure and the novel emerging features of the mesonic non-singlet spectrum of the Minimal Walking Technicolor (MWT) theory. Precision measurements in the nonsinglet pseudoscalar and vector channels are compared to the expectations for an IR-conformal field theory and a QCD-like theory. Our results favor a scenario in which MWT is (almost) conformal in the infrared, while spontaneous chiral symmetry breaking seems less plausible.

PACS numbers: 11.15.Ha, 12.60.Nz, 12.39.Pn

## I. INTRODUCTION

The idea of a new strong force in our model of Nature to explain Electro-Weak Symmetry Breaking (EWSB) dynamically was first suggested many years ago [1, 2]. Borrowing from our intuition of QCD, a new strong sector beyond the standard model was proposed in which chiral symmetry breaks down at the TeV scale leading to EWSB and providing an explanation for the observed gauge boson masses. Moreover, the standard model fermions acquire their masses via extended technicolor interactions. The first models based on these ideas were obtained by a naive rescaling of QCD, i.e. they were based on a  $SU(N)$  gauge theory with a small number of fundamental matter fields. Despite the elegance of the proposal, it was soon shown that such models are not viable candidates: together with the mass of SM particles, large Flavor Changing Neutral Currents (FCNC) and large values of the Peskin-Takeuchi [3, 4] parameters would also be generated. Electroweak precision tests performed at LEP [5] put tight experimental constraints on FCNC and the oblique parameters, which are incompatible with such predictions.

However, the naive rescaling arguments leading to the above conclusions can be flawed if the dynamics of the new sector is sufficiently different from QCD. In fact the intrinsic difficulty of handling strongly interacting models has not stopped the theoretical speculations. Walking and conformal technicolor theories have been proposed [6–9] whose large-distance dynamics is expected to be very different from the one of QCD. In particular it was shown that models falling in these frameworks could satisfy the experimental constraints (for recent reviews of technicolor models see [10–13]).

Good candidate models in these frameworks are those which lie close to the lower boundary of the so-called conformal window, where the presence of an (approximate) IR fixed point is believed to significantly change the non-perturbative dynamics of the theory.

The use of matter fields in higher dimensional representations has been recently advocated [14, 15] as an effective and economic way of satisfying all known experimental constraints.

In this work we will focus on one of these candidate theories, the so-called Minimal Walking Technicolor theory, based on the gauge group  $SU(2)$  with two Dirac fermions in the adjoint representation.

All viable candidate models share the common property of being strongly interacting at the electroweak scale and as such are not fully under control by analytic methods only. Although the analytical approaches are indispensable to show which models are the most promising, they all depend on uncontrolled approximations or conjectures based on educated guesses.

In this work we study MWT using first-principle numerical simulations, which allow to investigate the full non-perturbative dynamics of the theory. We use the same techniques matured during the last decades for Lattice QCD and which are now source of reliable and valuable informations for the phenomenology of the strong interactions at high-energy experiments. Within the Lattice Gauge Theory framework quantitative predictions can be obtained, which demonstrate if a candidate model is indeed viable or not.

In the last two years renewed interest among the lattice community has led to an increasing number of studies by several different groups [16–55].

In this work we present a detailed study of the non-singlet mesonic sector of the spectrum of the gauge theory  $SU(2)$  with two Dirac adjoint fermions. In a companion paper [56] we will present our result for the glueball mass spectrum and string tension and compared them to the one obtained in this paper for the mesonic spectrum as first suggested in [42]. As the simplest of such interesting models, it is particularly amenable to numerical investigations.

\*luigi.del.debbio@ed.ac.uk

†b.lucini@swansea.ac.uk

‡a.patella@swansea.ac.uk

§pica@cp3.sdu.dk

¶rago@physik.uni-wuppertal.de

Given the present analytical uncertainties, it is not clear if this theory lies within the conformal window or not. To understand if this model lies within the conformal window, in this paper we will compare our data to the signatures of spontaneous chiral symmetry breaking on the one hand and to the expected scaling behavior in proximity of an IR fixed point on the other. By studying the dependence of the low-lying meson masses on the current quark mass we will provide evidence for the existence of an IR fixed point.

This paper is organized as follows. In Sect. II we remind to the reader the physical implications of the existence of an IR fixed point in the theory and its observable consequences as derived from a Renormalization Group (RG) analysis of the fixed point. In Sect. III we introduce the Lattice Gauge Theory formalism used in this work. In Sect. IV we present our numerical results and compare them to the theoretical expectations. We finally conclude in Sect. V.

## II. NON-QCD BEHAVIOR

Strongly interacting theories that have a dynamics different from QCD are needed in order to be able to build successful phenomenological models of DEWSB. One example of such theories is provided by gauge theories in the so-called *conformal window*, which are characterized by the existence of an infrared fixed point in their renormalization group flow.

A four-dimensional gauge theory minimally coupled to fermions in some representation of the gauge group has a perturbative UV fixed point provided the number of fermion species is not too large; at the UV fixed point the gauge coupling  $g$  and the fermion mass  $m$  are relevant couplings. The gauge coupling  $g$  is dimensionless in four dimensions. It is convenient to use dimensionless couplings for discussing RG flows. Hence we shall consider the dimensionless quantity  $\hat{m} = am = m/\mu$  when studying the RG transformations of the fermion mass. Renormalized trajectories, *i.e.* lines of constant physics, are one-dimensional curves originating from the UV fixed point. Points on a given renormalized trajectory correspond to theories that have the same long-distance physics, but different values of the UV cutoff. Each line corresponds to a theory with a given physical fermion mass.

One of the lines of constant physics corresponds to the massless renormalized trajectory. If the theory possesses an IRFP, the latter has to lie on the massless trajectory, otherwise the finite fermion mass would drive the theory away from the IRFP at large distances. Assuming the existence of such a fixed point, we can linearize the RG equations in the vicinity of the fixed point, and identify relevant and irrelevant directions. In particular the mass  $\hat{m}$  will be a relevant operator.

The running of the couplings is described by the RG

equations:

$$\mu \frac{d}{d\mu} g = \beta(g), \quad (1)$$

$$\mu \frac{d}{d\mu} m = -\gamma(g)m, \quad (2)$$

where  $g$  and  $m$  are respectively the running coupling and the running mass, which depend on the energy scale  $\mu$ . Note that chiral symmetry guarantees that the RHS of Eq. (2) is proportional to the mass itself. The function  $\gamma$  is the anomalous dimension of the scalar density operator  $\bar{\psi}(x)\psi(x)$ . Eq. (2) implies:

$$\mu \frac{d}{d\mu} \left( \frac{m}{\mu} \right) = -[\gamma + 1] \left( \frac{m}{\mu} \right). \quad (3)$$

Similar equations describe the evolution of all the other couplings that are compatible with the symmetries of the system under study. We shall denote the generic, dimensionless coupling  $\hat{g}_i$ ; their evolution is dictated by a corresponding  $\beta$  function:

$$\mu \frac{d}{d\mu} \hat{g}_i = \beta_i(\hat{g}). \quad (4)$$

The IRFP is defined by an isolated zero of the  $\beta$  functions. Theories in the conformal window become scale-invariant at large distances, and therefore cannot develop condensates. In particular chiral symmetry cannot be spontaneously broken, and there are no single-particle states; the dynamics is entirely expressed by the exponents that characterize the power-law behavior of field correlators at large distances.

In the vicinity of a fixed point  $\hat{g}^*$  the RG equations can be linearized; the evolution is characterized by the matrix:

$$R_{ij} = \left. \frac{\partial \beta_i}{\partial \hat{g}_j} \right|_{\hat{g}^*}. \quad (5)$$

The evolution of the dimensionless eigenvectors of the matrix  $R$ ,  $u_i$ , is given by simple power laws:

$$u_i(\mu) \propto \mu^{-y_i}, \quad (6)$$

where  $y_i$  are the eigenvalues of  $R_{ij}$ . The  $y_i$  are the critical exponents that are commonly used in the theory of critical phenomena. It is clear from Eq. (6) that  $y_i > 0$  characterizes the relevant directions at the IRFP.

The fermion mass is a relevant operator at the fixed point, and we can readily deduce from Eq. (3):

$$y_m = \gamma_* + 1, \quad (7)$$

where  $\gamma_*$  is the value of the anomalous dimension at the fixed point.

The scaling (or conformal) dimension of the scalar density  $\Delta_m$  is related to the critical exponent  $y_m$  by:

$$y_m = D - \Delta_m, \quad (8)$$

where  $D$  is the dimension of space-time. The scaling dimension for a scalar operator is bound to be greater than one by unitarity, and it is equal to three for the scalar density in the free theory. This corresponds to the usual range  $0 \leq \gamma_* \leq 2$ .

**Scaling of the free energy density.** Let us now consider a RG transformation such that the lengths are rescaled by a factor  $b$ :

$$a' = ba, \quad \mu' = \mu/b. \quad (9)$$

Following the discussion above, the transformation of the singular part of the free energy density under such transformation can be written as:

$$f_s(u_i, am, a/L) = b^{-D} f_s(b^{y_i} u_i, b^{y_m} am, ba/L). \quad (10)$$

We have denoted by  $u_i$  the irrelevant operators at the

IRFP, and therefore  $y_i < 0$ , while  $y_m > 0$  as expected from the discussion above on the role of the fermion mass. We have included the dependence on the size of the box  $L$ , since this will provide finite-size scaling laws. The inverse of the size  $1/L$  is treated as relevant coupling with unit eigenvalue; the underlying hypothesis here is that the finite value of  $L$  does not affect the RGE for the other couplings, *i.e.* that it is larger than the inverse mass of the states in the theory,  $Lm \ll 1$ .

Iterating the RG transformation  $n$  times yields:

$$f_s(u_i, am, a/L) = b^{-nD} f_s(b^{ny_i} u_i, b^{ny_m} am, b^n a/L). \quad (11)$$

Choosing  $n$  such that  $b^{ny_m} am = am_0$ , where  $m_0$  is some reference mass scale, Eq. (11) can be rewritten as:

---


$$f_s(u_i, am, a/L) = \left(\frac{m}{m_0}\right)^{\frac{D}{y_m}} f_s\left(\left(\frac{m}{m_0}\right)^{-\frac{y_i}{y_m}} u_i, am_0, \left(\frac{m}{m_0}\right)^{-\frac{1}{y_m}} a/L\right) = \left(\frac{m}{m_0}\right)^{\frac{D}{y_m}} \Phi\left(mL^{y_m}, \left(\frac{m}{m_0}\right)^{\frac{|y_i|}{y_m}} u_i\right). \quad (12)$$


---

Eq. (12) describes the scaling with the fermion mass, and the functional form of finite-size effects. Expanding  $\Phi$  in powers of  $x_i = \left(\frac{m}{m_0}\right)^{|y_i|/y_m} u_i$ , assuming as usual that  $f_s$  is analytic as a function of the irrelevant couplings, yields the corrections to the scaling. Note that these corrections vanish when  $x = 0$ .

Ignoring the corrections to scaling we obtain an expression for the free energy that is useful to derive finite-size scaling properties:

$$f_s(am, a/L) = \left(\frac{m}{m_0}\right)^{D/y_m} \Phi(mL^{y_m}). \quad (13)$$

**Scaling of correlators.** Two-point function correlators:

$$f_H(x; am) = \int d^{D-1} x \langle H(x) H(0)^\dagger \rangle \quad (14)$$

satisfy similar RG equations:

$$\left[ a \frac{\partial}{\partial a} - \gamma_m \frac{\partial}{\partial m} - 2\gamma_H \right] f_H(x; am) = 0, \quad (15)$$

where we have neglected the dependence on the irrelevant couplings, and  $\gamma_H$  is the anomalous dimension of the field  $H$ . The solution to the above equation obeys the following scaling law:

$$f_H(x; am) = b^{-2\gamma_H} G(x; b^{y_m} am), \quad (16)$$

Iterating this relation  $n$  times, and performing manipulations analogous to the ones above, yields:

$$f_H(x; am) = \left(\frac{m}{m_0}\right)^{2\gamma_H/y_m} \Psi\left(x/|m/m_0|^{-1/y_m}\right). \quad (17)$$

If the correlator decays exponentially at large distances with the mass of the lightest state that overlap with the fields, then Eq. (17) determines the scaling of this mass:

$$M \sim m^{1/y_m}. \quad (18)$$

Using the relation between  $y_m$  and  $\gamma_*$  discussed above, the scaling for the masses of the physical states is

$$M \sim m^{1/(1+\gamma_*)}. \quad (19)$$

Note that according to this analysis all masses scale with the same exponent. Different states are selected by different fields appearing in the correlator  $f_H$ , which implies that the anomalous dimension in the prefactor,  $y_H$ , does change. However the scaling of the mass is entirely due to the RG behavior of the argument of the function  $\Psi$ , which does not depend on the state under scrutiny.

### III. LATTICE SIMULATIONS

Non-perturbative numerical simulations are performed after introducing an effective UV and IR cutoff in the form of a space-time lattice of finite extent.

The Euclidean path integral is thus reduced to an ordinary integral over a large number of degrees of freedom. The choice of a discretized action on the lattice is not unique; different choices will result in different lattice artefacts. Unimproved Wilson fermions are used throughout this work. The lattice action with matter fields in a representation  $R$  is given by<sup>1</sup>

$$S(U, \psi, \bar{\psi}) = S_g(U) + \sum_{i=1}^{n_f} \bar{\psi}_i D_m(U^R) \psi_i, \quad (20)$$

with explicit expressions for the gauge action  $S_g$  and the massive lattice Dirac operator  $D_m$  given below. For this choice of discretization, the action depends only on two bare parameters: the bare inverse coupling  $\beta$  and the bare dimensionless quark mass  $am_0$ ,  $a$  being the lattice spacing. While the link variables appearing in the gauge action are in the fundamental representation<sup>2</sup> of the gauge group, the links in the lattice Dirac operator are in the same representation  $R$  as the fermion fields. The partition function, after integrating out the matter fields, takes the form:

$$Z = \int \exp[-S_g(U)] [\det D_m(U^R)]^{n_f} dU. \quad (21)$$

For the Wilson action used in this work the gauge action is given by

$$S_g(U) = \frac{\beta}{N_c} \sum_{x, \mu < \nu} \text{Re tr } \mathcal{P}_{\mu\nu}(x), \quad (22)$$

where  $\mathcal{P}_{\mu\nu}(x)$  is the elementary  $1 \times 1$  plaquette in the  $\mu$ - $\nu$  plane at lattice site  $x$ . In the fermion action the Wilson-Dirac operator is given by

$$D_m(U^R) = am_0 + \frac{1}{2} \sum_{\mu} [\gamma_{\mu} (\nabla_{\mu} + \nabla_{\mu}^*) - a \nabla_{\mu}^* \nabla_{\mu}], \quad (23)$$

where  $\nabla_{\mu}$  is the discretized forward covariant derivative depending on the link  $U_{\mu}^R$  and  $\nabla_{\mu}^*$  its adjoint operator:

$$(\nabla_{\mu} \psi)(x) = U^R(x, \mu) \psi(x + \mu) - \psi(x). \quad (24)$$

In a numerical lattice simulation the computation of the discretized path integral is performed by Monte Carlo integration using importance sampling: an *ensemble* of gauge configurations is generated with probability proportional to  $\exp[-\beta S_g(U)] [\det D_m(U^R)]^{n_f}$ . The expectation value of any observable can then be computed as a stochastic average over this ensemble of configurations.

## A. Sources of systematic errors

In order to obtain continuum values for the observables of a theory from numerical simulations of its lattice discretised version, an appropriate limiting procedure must be performed. It is thus important to understand when and to what extent the outcome of lattice simulations are a faithful depiction of the continuum physics. This is especially important when one tries to understand a new theory as the MWT in the present work, since we lack the insight and the experimental input we have for instance in the more familiar case of QCD. In fact, in order to be the description of a new force of Nature, this theory has to be rather different from QCD and we need to ensure that we are observing genuine features of the continuum theory, and not artefacts of our lattice formulation.

We will now list the most important sources of systematic errors which are present in lattice simulations and what are the appropriate limits to take in order to recover the continuum physics. In addition to these, statistical errors are also always present, but those can be reduced arbitrarily by producing a big enough ensemble of configurations.

**Finite-size, finite-temperature effects.** These are due to the presence of an IR cutoff in the form of a finite extent of the 4-dimensional lattice both in the spacial and temporal directions. The standard lattice geometry used in numerical simulations is  $T \times L^3$ , i.e. the three spacial directions have equal length. The correct vacuum expectation values of the continuum theory are recovered in the limit in which  $T, L \rightarrow \infty$ . On a 4-dimensional torus these expectation values can have large corrections, even if asymptotically the infinite volume limit is reached at an exponentially fast rate. As the system is tuned closer to a critical point, the magnitude of finite-size effects and the autocorrelation of lattice observables increase. This is what happens for example when particles with a Compton wavelength comparable with the lattice size are present. Moreover, if the size of the lattice is not sufficiently large, the system may enter a phase that bears little resemblance to the large-volume theory we are interested in. Some examples, based on analytical finite-volume results [57–59], have been recently discussed in Ref. [43].

**Explicit breaking of chiral symmetry.** It is difficult and numerically very expensive to preserve chiral symmetry once the theory is discretized on a lattice. For the particular choice of the lattice action used in the work, i.e. Wilson-Dirac fermions, chiral symmetry is explicitly broken at the Lagrangian level. In order to recover it in the continuum limit the tuning of one parameter (the bare quark mass) is necessary. Even with lattice chiral fermions, the low modes of the lattice Dirac operator, which appear as the chiral limit is approached, make it practically impossible to run simulations at very light masses with the current algorithms. When using Wilson fermions on a given finite lattice, there is a lower limit to the masses that are numerically accessible. This

<sup>1</sup> We omit for the sake of simplicity all the position, color and spin indexes.

<sup>2</sup> The link variables can also be taken in a different representation of the gauge group if one chooses to.

limit depends on the volume of the system [60, 61].

**Discretization artefacts.** The space-time lattice introduces a UV cutoff, i.e. the lattice spacing  $a$ . The interesting continuum physics is recovered in the limit where the lattice spacing goes to zero. However since all the quantities in a simulation are dimensionless, the lattice spacing  $a$  is not a parameter that one can directly change. Instead the value of the lattice spacing is inferred from the measure of a physical quantity on the lattice, which is thus used to fix the scale  $a$ . The continuum limit is recovered when the system is tuned to a UV critical point where the lattice spacing vanishes. This can be done in the space of bare parameters by increasing the lattice inverse coupling  $\beta$  to infinity, i.e. sending the coupling of the theory  $g$  to zero, as dictated by asymptotic freedom. At that point the system undergoes a continuous phase transition and, by universality, the microscopic details of the system become immaterial. To put it in a different way, the physics at the scale of the lattice spacing must decouple from the long range (continuum) physics, which is what we are interested in studying on the lattice.

To give reliable predictions, lattice simulations must be performed in a regime in which a precise hierarchy of scales is realized. To illustrate this point, let us consider first the case of QCD. Numerical simulations, as explained above, are always performed with a finite quark mass, which explicitly induces a mass gap in the theory. To avoid finite-size effects in the computation of the low-lying spectrum, the lattice size  $L$  must be much bigger than the inverse mass of the lightest hadron  $M_{\text{PS}}$  we aim to measure. If we are interested in the chiral regime, as it is usually the case, this light hadron mass must be much smaller than the characteristic hadronic scale at which the theory becomes strongly interacting. In QCD we can take for example the Sommer scale  $r_0$  as a convenient quantity to measure on the lattice. Finally to avoid discretization errors, the lattice spacing must be much smaller than the reference scale for strong interactions  $r_0$ , so that the physics at the scale of the UV cutoff is weakly interacting. In summary we must have the following hierarchy of scales:

$$L^{-1} \ll M_{\text{PS}} \ll r_0^{-1} \ll a^{-1}, \quad (25)$$

for the computations to reproduce reliably the features of the continuum chiral regime of QCD.

Let us now consider the case in which the underlying continuum theory has an IR fixed point in the massless limit. The presence of a mass term in numerical simulations explicitly breaks conformal invariance and as in the QCD-like case a mass gap and a particle spectrum for the theory are generated. In order to reliably estimate a hadron mass, we still need the lattice to be big enough to fit the state we are interested to measure, i.e. as above  $L^{-1} \ll M_{\text{PS}}$ , for example. However in contrast to the QCD-like case, all the masses of the hadrons vanish as we send the explicit symmetry breaking term to zero. One can still define an IR scale like  $r_0$  but, as the theory

is no longer confining,  $r_0$  is no longer related to the particle masses and it is therefore not a useful quantity to compare to. One can be tempted however to introduce a modified version of the IR scale  $\Lambda$  which marks the onset of the IR scaling region. With this definition the interesting mass region to explore is  $M_{\text{PS}} \ll \Lambda$ , in analogy with the previous case. Finally also in this case discretization artefacts should be suppressed using fine lattices. In summary we have a similar hierarchy of scales as before

$$L^{-1} \ll M_{\text{PS}} \ll \Lambda \ll a^{-1}, \quad (26)$$

with a new IR scale  $\Lambda$  whose definition is related to the new features of the theory. Unfortunately a convenient definition of  $\Lambda$  readily measurable on the lattice, like the Sommer scale for QCD, is not at hand. As defined above  $\Lambda$  can only be inferred *a posteriori* by observing the scaling behavior of some physical observable.

## B. Simulation Code

The results presented in this work are obtained using our own simulation code, written from scratch for the specific purpose of studying gauge theories with fermions in arbitrary representations. The code was developed during the last few years and has been presented and tested in detail in Ref. [21]. This code was designed to be flexible and easily accommodate for fermions in arbitrary representations of the gauge group, without compromising the performance and ease of use of the code itself.

Our simulation code, named HiRep, is suitable for the study of gauge theories with

- gauge group  $SU(N)$  for any  $N$ . The code has already been used for the study of the large- $N$  mesonic spectrum [62] with  $N$  up to 6.
- generic fermion representations. At present the code implements the fundamental (fund), adjoint (ADJ), 2-index symmetric (S) and antisymmetric (AS). All of these different representation have already been successfully tested and used [63]. It is easy to extend the code to other representations, like 3-index symmetric for example, and even to have fermions in two or more different representations at the same time. In particular no modifications for the computation of the HMC force are needed, which is typically the most complicated part of the code.
- any number of flavors. We use Wilson fermions with the HMC[64]/RHMC[65, 66] algorithm, which is an exact algorithm for any number of flavors.

We have also implemented a significant number of observables such as the the measure of the mesonic spectrum (presented in this work), Schrödinger functional observables (used in Ref. [48]), gluonic observables like Wilson

and Polyakov loops, glueball masses presented in a companion paper [56].

Since this was a new code, and lattice simulations in the past were mainly devoted only to QCD, we made a large effort to validate the code and to study its behavior in the parameter region of interest for the physics. As part of this effort, in particular we made a number of cross-checks:

- for  $SU(3)$ ,  $n_f = 2$  with different, established codes (we used M. Luscher's DD-HMC algorithm [67]);
- consistency among different representations (e.g.  $SU(3)$  AS vs fund,  $SU(2)$  SYM vs ADJ);
- observables with different codes (e.g. meson spectrum for  $SU(2)$  ADJ in Chroma);
- large quark mass limit compared to pure gauge (quenched) spectrum;
- correctness of integrator, reversibility, acceptance probability;
- independence from integrator step size.

To control the stability of the simulations, which could incur in well-known problems close to the chiral limit [60], we monitored the lowest eigenvalue of the (pre-conditioned) Wilson-Dirac matrix. The average value of the lowest eigenvalue together with the standard deviation of their distribution can be found in the tables in Appendix B. We found no instabilities in our runs.

### C. Meson masses

Let  $\Gamma$  and  $\Gamma'$  be two generic matrices in the Clifford algebra, we define the two-point correlator at zero momentum as follows:

$$f_{\Gamma\Gamma'}(t) = \sum_{\mathbf{x}} \langle (\bar{\psi}_1(\mathbf{x}, t) \Gamma \psi_2(\mathbf{x}, t))^\dagger \bar{\psi}_1(0) \Gamma' \psi_2(0) \rangle, \quad (27)$$

where  $\psi_1$  and  $\psi_2$  represent two different flavors of degenerate fermion fields, so that we only consider flavor non-singlet bilinears. Denoting the space-time position  $(\mathbf{x}, t)$  by  $x$  and performing the Wick contractions yields:

$$f_{\Gamma\Gamma'}(t) = \sum_{\mathbf{x}} -\text{tr} [\gamma_0 \Gamma^\dagger \gamma_0 S(x, 0) \Gamma' S(0, x)], \quad (28)$$

where  $S$  denotes the quark propagator, i.e. the inverse of the hermitean Wilson-Dirac matrix  $\gamma_5 D$ . In practice not all matrix elements of  $S$  are computed, but only some single rows (point-to-all propagator) by solving the linear system:

$$D(x, y)_{AB} \eta_B^{\bar{A}, 0}(y) = \delta_{A, \bar{A}} \delta_{x, 0}, \quad (29)$$

where capital Latin letters like  $A = \{a, \alpha\}$  are collective indices for color and spin, and  $\bar{A}$ ,  $x = 0$  is the position

of the source for the inverter. The inversion is performed using a QMR recursive algorithm with even-odd preconditioning of the Dirac operator, which is stopped when the residue is less than  $10^{-8}$ . For some of our lattices we used the noise-reduction technique described in Ref. [68] to take a stochastic average over the volume of the point source.

Following Ref. [61], masses and decay constants for the pseudoscalar meson are extracted from the asymptotic behavior of the correlators  $f_{PP}$  and  $f_{AP}$  at large Euclidean time. The pseudoscalar mass and the vacuum-to-meson matrix element are obtained from the correlator of two pseudoscalar densities:

$$f_{PP}(t) = -\frac{G_{PS}^2}{M_{PS}} \exp[-M_{PS}t] + \dots \quad (30)$$

The meson mass is obtained by fitting the effective mass to a constant, while the coupling  $G_{PS}$  is extracted from the amplitude of the two-point function  $f_{PP}$ . The definition of the effective mass used in this work is given in Appendix A.

As in Ref. [61] the ratio

$$m_{\text{eff}}(t) = \frac{1}{4} [(\partial_0 + \partial_0^*) f_{AP}(t)] / f_{PP}(t) \quad (31)$$

yields the PCAC mass  $m$  with corrections of  $\mathcal{O}(a)$  for the unimproved theory. Note that the decay constant is not computed directly; it is obtained from the values computed above as:

$$F_{PS} = \frac{m}{M_{PS}^2} G_{PS}. \quad (32)$$

The decay constant extracted from bare lattice correlators is related to its continuum counterpart by the renormalization constant  $Z_A$ , which has been computed in perturbation theory in Ref. [18].

Finally the mass of the vector state is extracted from the  $f_{VV}$  correlator, again using a fit to the effective mass plateaux.

On the smallest lattices that we have used in this study, it is difficult to isolate clearly the contribution from the lowest state, which dominates the large-time behavior of two-point correlators; this yields large systematic errors. We have however explicitly measured the meson masses at the same value of the bare parameters – corresponding to the same value of the PCAC mass – on increasingly larger lattices to ensure that the residual finite-volume corrections on these quantities are small.

For the pseudoscalar and vector channels we have also verified that different choices of interpolating operators give results that agree with each other. In these channels the final results presented below are obtained taking the average over the different choices of interpolating operators.

### D. Simulation parameters

All the simulations discussed in this work are performed at a fixed lattice spacing, corresponding to a bare coupling  $\beta = 2.25$ . This value of the coupling was chosen based on previous studies of the same theory [16, 22, 34] to avoid a bulk phase transition present at about  $\beta = 2.0$ . The extrapolation towards the continuum limit requires a new series of runs at different values of the bare coupling, and is left to future investigations.

We use four different lattices:  $16 \times 8^3$ ,  $24 \times 12^3$ ,  $32 \times 16^3$  and  $64 \times 24^3$ . For each of these four lattices a number of ensembles corresponding to different quark masses were generated, focusing in particular on the range corresponding to pseudoscalar masses between  $0.6a^{-1}$  and  $0.2a^{-1}$ . As explained above, when using Wilson fermions, the chiral and infinite volume limits are intertwined. In practice for the simulation to be stable, one cannot arbitrarily decrease the quark mass without also increasing the volume. This is also necessary to keep under control finite-volume effects, thus remaining in the large volume limit. We explicitly control the size of these systematic errors performing simulations with different volumes.

For each lattice and quark mass we accumulated a statistical ensemble of about 5000 thermalized configurations, except at the largest volume for which we present only preliminary data based on approximately 500 configurations for each quark mass. The gauge configurations were generated using trajectories in the molecular dynamics integration of length 1 for the two smallest volumes and 1.5 for the two largest lattices, with integration parameters leading to an acceptance rate of about 85% in all cases, and to an integrated autocorrelation times for the lowest eigenvalue of the Wilson–Dirac operator of order 15 or less.

Details of simulation parameters and results are reported in the tables of Appendix B.

## IV. SU(2) WITH 2 ADJOINT FERMIONS

Before looking at the actual numerical results, let us discuss the signatures of an IR fixed point, in order to focus on the important aspects of our numerical evidence. In this work, we search for indications of IR conformal behavior in the spectrum. This is not the only possible way, as one can, for example, study the non-perturbative running of a coupling defined in some particular scheme. In fact most of the claims of the existence of IR fixed points so far have been made by looking at the evolution of the coupling in the Schrödinger functional scheme [17, 19, 36, 48]. However at present these studies still lack a reliable continuum extrapolation and the claims of the existence of IR fixed points should therefore be confirmed by more solid numerical investigations.

If there is no IR fixed point, the theory is expected to be confining and chiral symmetry to be spontaneously broken. We will refer to this case as QCD-like: in the

chiral limit the pseudo-scalar particles (pions) become massless, while the other states in the spectrum remain massive. In the small mass regime the theory can be effectively described by a chiral lagrangian and the familiar results of QCD can be recovered. In particular the theory has a non-zero pseudoscalar decay constant  $F_{\text{PS}}$  and chiral condensate  $\langle \bar{\psi}\psi \rangle$ . Using the PCAC mass from the axial Ward identity,  $m$ , to parametrize the explicit breaking of chiral symmetry, we expect the usual scaling  $M_{\text{PS}}^2 \propto m$ , as  $m \rightarrow 0$ . The Gell-Mann–Oakes–Renner relation is satisfied and can be used to extract the chiral condensate:  $(M_{\text{PS}}F_{\text{PS}})^2/m \rightarrow -\langle \bar{\psi}\psi \rangle$ .

On the other hand, if the theory has an IR fixed point, the arguments of Sect. II apply. In the scaling region, i.e. in proximity of the IR fixed point, dimensionful physical quantities are expected to scale with a power law behavior. The universal exponents appearing in these scaling laws are related to the anomalous dimensions of the scaling fields as shown in Sect. II. In particular the scaling of the hadron masses is governed by the anomalous dimension of the mass  $\gamma_*$  at the fixed point. If we parametrize the explicit breaking of chiral and conformal symmetry by  $m$ , in the massless limit  $m \rightarrow 0$  we expect that all hadron masses vanish proportionally to the same power of  $m$ :  $M_{\text{had}} \sim m^{1/(1+\gamma_*)}$ ; in particular the ratio of the vector to pseudoscalar meson masses remains finite:  $M_V/M_{\text{PS}} \rightarrow \text{const} < \infty$ . Also the pseudoscalar decay constant  $F_{\text{PS}}$  and the chiral condensate  $\langle \bar{\psi}\psi \rangle$  are expected to vanish in the chiral limit.

The behavior just described assumes that the system is in an infinite volume near the continuum limit. However this is not always the case in a lattice simulation. In particular the finite size of the system can be seen as a relevant coupling which will drive the system away from criticality under the renormalization group (RG) flow. As  $m$  is decreased towards the chiral limit, great care must be taken to control finite size effects as explained in Section III. We will show below that these effects are quite big in the range of masses and lattice volumes which are currently used in numerical simulations.

### A. Spectrum

For each ensemble of configurations, we measured the quark mass from the axial Ward identity (PCAC mass)  $m$ , the pseudoscalar meson mass  $M_{\text{PS}}$ , the vector mass  $M_V$  and the pseudoscalar decay constant  $F_{\text{PS}}$ .

We locate the chiral limit at the critical bare mass where the PCAC mass vanishes. This does not correspond to zero bare mass because the explicit breaking of chiral symmetry with Wilson fermions induces an additive renormalization of the quark mass. We show in Fig. 1 the extrapolation of  $m$  for different lattice sizes. Using a linear extrapolation of the four lightest measured points, the chiral limit can be located at the critical bare mass  $am_c = -1.202(1)$ . As expected from the fact that  $m$  is an UV quantity, no significant finite-size effects are

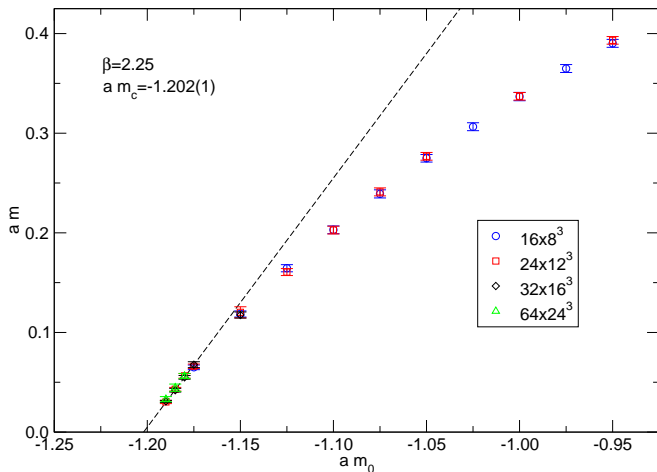


FIG. 1: Extrapolation of the quark mass from the axial Ward identity to locate the chiral limit. As expected no significant finite size effects are present.

visible and the measured values for this quantity agree within errors on all four lattices.

Our results for the mass of the pseudoscalar meson are presented in Fig. 2. The interesting region of small quark masses is shown in the right panel. Given the level of accuracy of the present measure, the finite volume systematics on  $M_{PS}$  are clearly visible and, as the PCAC mass is decreased, they become more and more relevant, as discussed in Sect. III. To quantify this systematic effect and to keep it under control, we use larger lattices as the chiral limit is approached.

These large finite size effects make it harder to draw definitive conclusions about the functional behavior of the pseudoscalar mass in the chiral limit. For a QCD-like theory the ratio  $aM_{PS}^2/m$ , shown in Fig. 3, should be a (non-zero) constant in the chiral limit. On the other hand if the theory has an IR fixed point the ratio should vanish in the chiral limit if  $\gamma_* < 1$  or diverge if  $\gamma_* > 1$ . Our data clearly favor the IR conformal scenario with  $\gamma_* < 1$ . An accurate determination of the anomalous dimension is more difficult, but from the almost linear behavior of  $M_{PS}$  as a function of  $m$  a small value of  $\gamma_*$  seems to be preferred.

The IR conformal scenario is also favored when one looks at the ratio of the vector to the pseudoscalar mass which is shown in Fig. 4. This quantity is bounded to be greater than 1 [69] and in the heavy quark limit will approach unity. At large  $m$  finite volume effects are small, the ratio is bigger than 1 and decreasing as  $m$  increases, as expected in the heavy quark approximation. What is remarkable in our data is the fact that in the whole mass range we were able to explore, and in which the pseudoscalar mass changes roughly by a factor of 7, the vector meson never becomes more than 5% heavier than the pseudoscalar, so that the ratio remains approximately constant in the chiral limit. This is the expected behavior in an IR conformal theory, since in this case all the

hadronic masses scale with the same critical exponent.

Another physically interesting quantity to consider is the pseudoscalar decay constant  $F_{PS}$ , shown in Fig. 5. Among the ones presented in this paper, this is the quantity which shows the largest sensitivity to finite-volume effects. By looking at the behavior of  $F_{PS}$  at different volumes, an envelope of the curves as a function of the PCAC mass is clearly visible, which should be used for the chiral extrapolation. For a QCD-like theory the result in the chiral limit is a non-zero value. The direct extrapolation however is difficult to carry out with reasonable accuracy; for this reason, we prefer to exploit the finite-size effects themselves to obtain a more insightful statement. As discussed in Sect. II near an IR fixed point one can consider the finite size  $L$  of the system as a relevant parameter in the RG flux and thus obtain universal scaling laws for physical observables, Eq. (13). This finite size-scaling law can be conveniently rewritten, for example for the pseudoscalar decay constant, as:

$$LF_{PS} = \Upsilon(Lm^{1/(1+\gamma_*)}). \quad (33)$$

Scaling is observed if the different curves corresponding to keeping the volumes fixed and varying the quark mass, collapse on top of each other. As a byproduct of the procedure an estimate of the critical exponent is also obtained. To illustrate the procedure, we plot  $LF_{PS}$  as a function of  $x = Lm^{1/(1+\gamma_*)}$  in Fig. 6 for various values of  $\gamma_*$ . Good scaling is observed for  $0.05 \leq \gamma_* \leq 0.20$ , while larger values of  $\gamma_*$  (and in particular  $\gamma_* = 1$ ) seem to be excluded. The observed scaling is again in agreement with the existence of an IR fixed point with a small  $\gamma_*$  in the MWT theory. The range of values of  $\gamma_*$  for which a good quality of the scaling is obtained is compatible with independent estimates performed with the Schrödinger functional [48].

A phenomenologically relevant quantity to look at is the ratio  $M_V/F_{PS}$ . This ratio is shown in Fig. 7. The large dependence of  $F_{PS}$  on the finite-size of the lattice is reflected in the large finite-size effects for the ratio. A tentative large-volume limit curve can be obtained by discarding the results at the lightest masses on the smaller volumes. As the fermion mass drops below  $0.1a^{-1}$ , the ratio starts decreasing unless the volume is made larger. Taking the envelope of the curves for different values of the volume, one can expect a value of about 5–6 in the chiral limit.

The chiral condensate would also be a prime candidate to study chiral symmetry breaking. However due to the use of Wilson fermions, the direct measure of  $\langle \bar{\psi}\psi \rangle$  is plagued with UV divergences which are notoriously difficult to tame. Using the GMOR relation an estimate for the chiral condensate can be obtained<sup>3</sup>. The method

<sup>3</sup> We do not attempt here to compute the necessary multiplicative renormalization constant, since we are not interested to the actual physical value. Perturbative results for the renormalization of fermions bilinears can be found in Ref. [18]



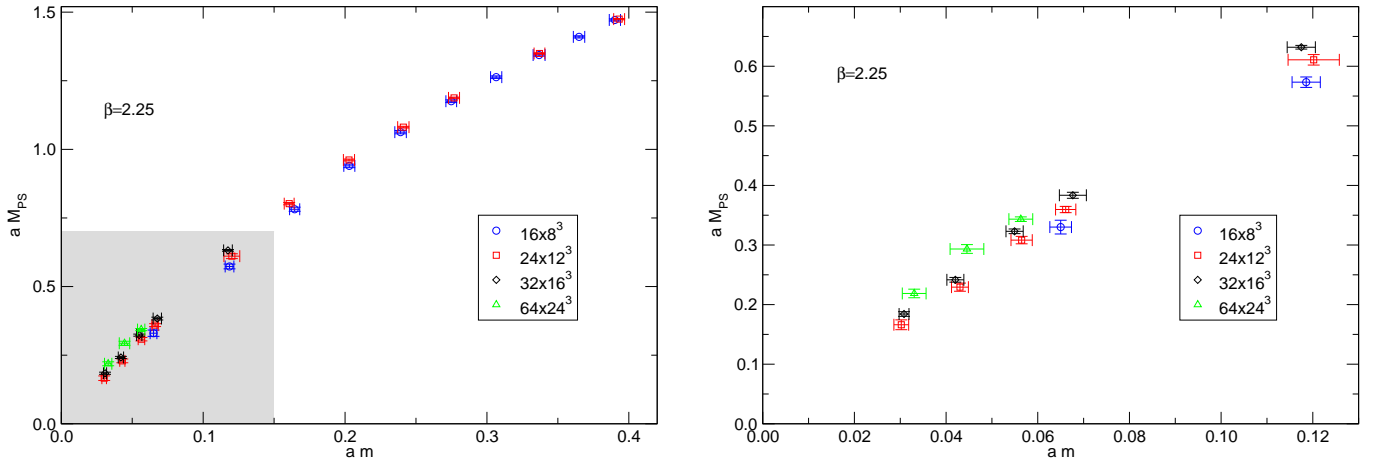


FIG. 2: Pseudoscalar meson mass as a function of the PCAC mass. The interesting small mass region shaded in the left panel is enlarged on the right. Finite volume effects are evident and grow approaching the chiral limit.

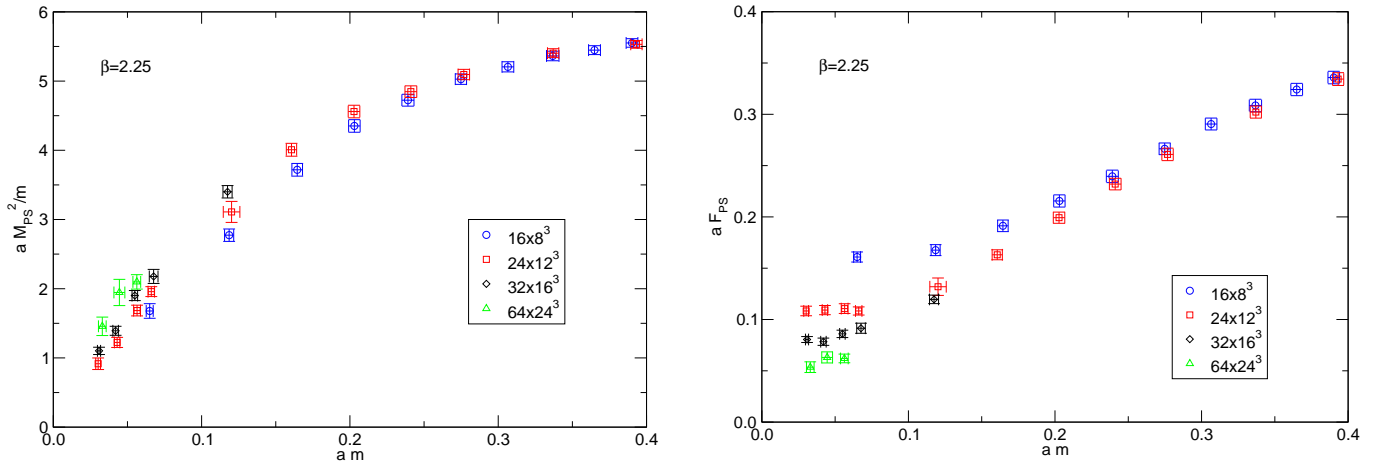


FIG. 3: Ratio of the pseudoscalar mass squared to the PCAC mass. The extrapolation to the chiral limit suffers from large finite-volume effects. See the text for a discussion.

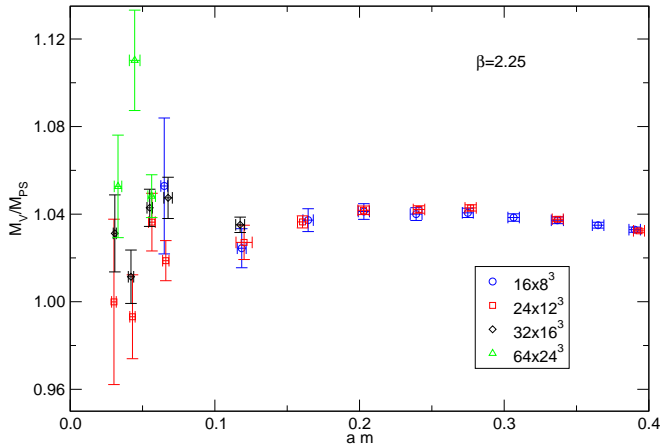


FIG. 4: Comparison between the vector and pseudoscalar meson masses. At large PCAC mass, due to quenching the ratio is very near to one. Near the chiral limit large finite size effects show up.

FIG. 5: Pseudoscalar decay constant near the chiral limit. Very large finite volume effects are present also in this case which cause the chiral extrapolation to be have large uncertainties.

has been applied with success in the case of QCD, see e.g. Ref. [70]. We present our results for this quantity in Fig. 8. Although there is a partial cancellation of the finite size effects coming from the pseudoscalar mass and the decay constant, the larger volume dependence of the latter dominates, yielding large systematic errors. As a consequence an extrapolation is unfortunately not possible from our current set of data. We observe that finite volume effects tend to make the condensate smaller, however the small numerical value of the bare condensate by itself is not meaningful: for example in a typical QCD simulation the value for this quantity is an order of magnitude smaller than the one presented here.

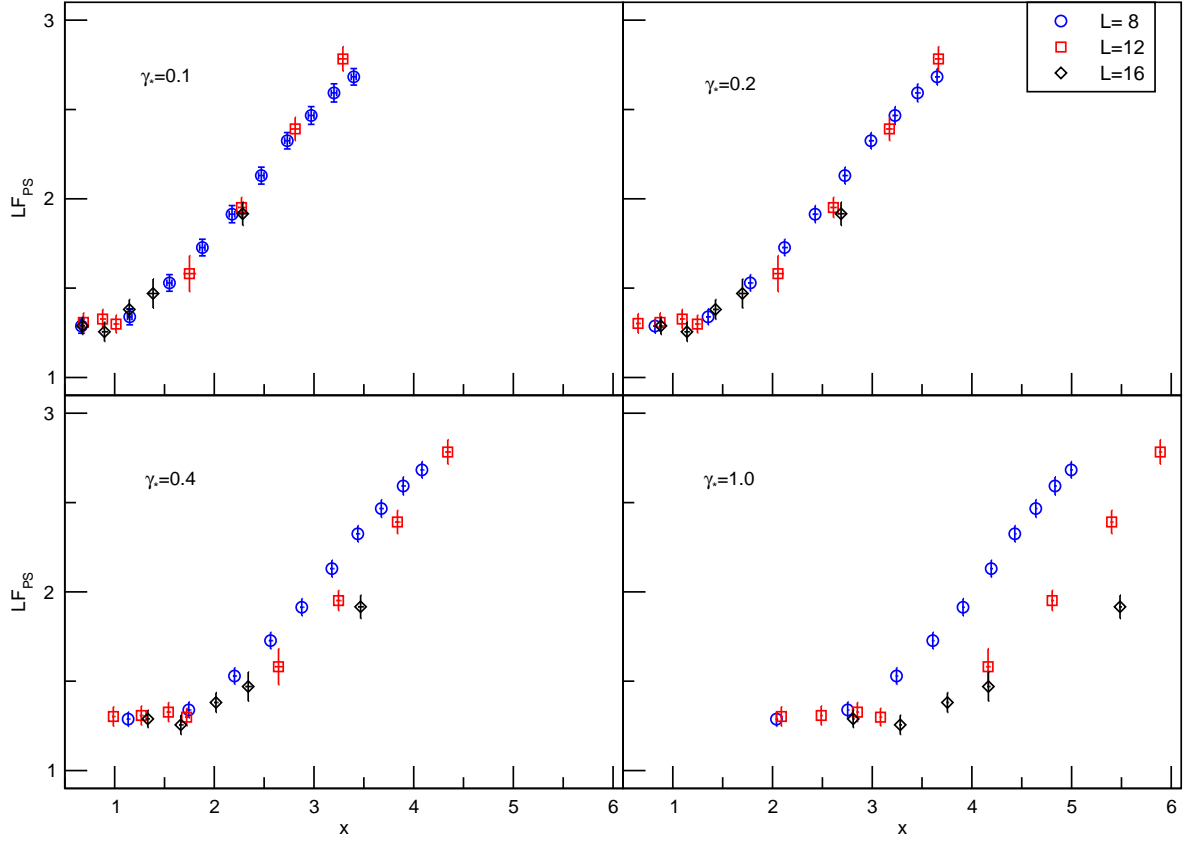


FIG. 6: Quality of the scaling of  $LF_{PS}$  as a function of  $x = Lm^{1/(1+\gamma_*)}$  for various values of  $\gamma_*$ .

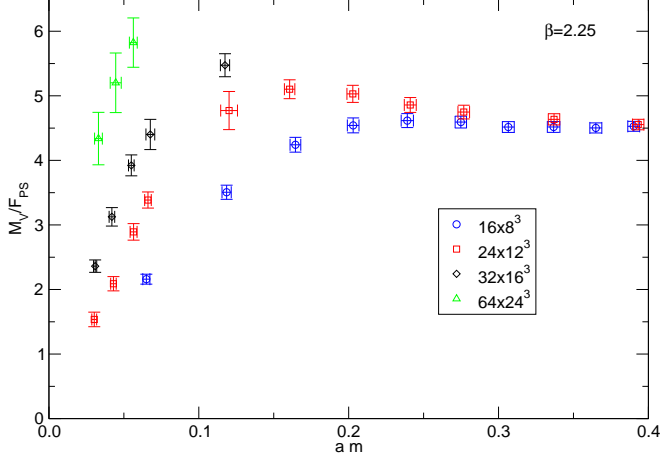


FIG. 7: Vector to pseudoscalar decay constant ratio. Large finite-size effects are present also in this case which make the extrapolation to the chiral limit difficult. The envelop of the curves in the plot suggests a limit value of about 5 – 6.

## V. CONCLUSIONS

In this work we have presented a careful investigation of the mesonic spectrum of one of the candidate theories for a realistic technicolor model, the so-called Min-

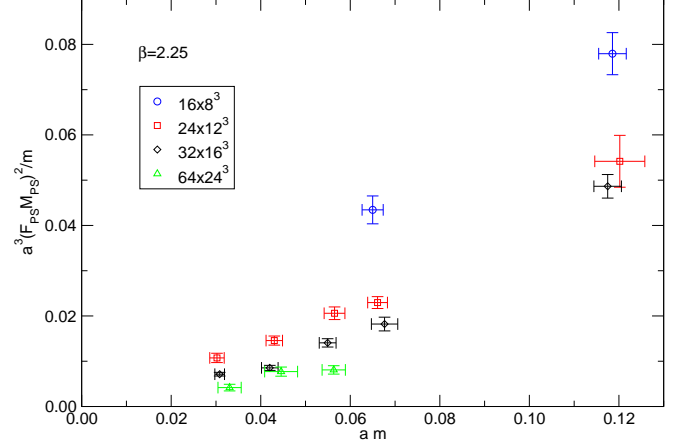


FIG. 8: The GMOR relation can be used to extract information on the chiral condensate. The measure results however quite difficult in practice and we cannot distinguish any signal of spontaneous chiral symmetry breaking.

imal Walking Technicolor, based on gauge group  $SU(2)$  with two Dirac adjoint fermions. Theoretical speculations about this theory indicate that it is very near to the lower boundary of the conformal window. In this work we used numerical lattice simulations to look at mesonic spectrum and we found some evidence that the theory

lies in fact inside the conformal window and possesses an IR conformal fixed point.

Such numerical simulations are an extremely powerful tool to explore the non-perturbative dynamics of gauge theories which is otherwise inaccessible to theoretical speculations, but great care must be taken to control systematic errors. In order to tame finite size corrections, which make the extrapolation to the chiral limit difficult, in this work we aimed for the first time at reaching the chiral limit in a controlled way: we used a series of four different lattice sizes up to a large  $64 \times 24^3$ .

Evidence for the existence of an IR fixed point was found in the behavior of the different mesonic observables analyzed, namely the pseudoscalar and vector meson mass and the pseudoscalar decay constant, which show significant deviations from the expectations of a more familiar QCD-like scenario, where spontaneous chiral symmetry breaking occurs. We showed that our data are compatible with the existence of an IR fixed point by using the predicted scaling laws that need to hold in this case.

Although the present data show clear signs of conformality in the infrared, our study still has several limitations which should be addressed in the future to put our results on a more solid ground. Smaller quark masses and consequently larger lattice volumes would increase the reliability of the scaling analysis we performed in this paper. However the major source of uncertainty is the fact that all numerical simulations used in this work were performed at a single value of the lattice spacing, and no test to assure the validity of our findings in the continuum limit has been done so far.

Finally in this paper we focused our attention only on the mesonic spectrum, while substantially more information can be gained by combining it with observables from other sectors of the theory, as we proposed in Ref. [42]. The detailed study of gluonic observables, and their comparison to the mesonic ones is the subject of a companion paper [56], which provides further evidence for the existence of an IR fixed point.

### Acknowledgments

The numerical calculations presented in this work have been performed on the BlueC supercomputer at Swansea university, on a Beowulf cluster partly funded by the Royal Society and on the Horseshoe5 cluster at the supercomputing facility at the University of Southern Denmark (SDU) funded by a grant of the Danish Centre for Scientific Computing for the project “Origin of Mass” 2008/2009. We thank C. Allton, J. Cardy, F. Knechtli, C. McNeile, M. Piai and F. Sannino for useful and fruitful discussions about various aspects related to this paper. We thank the organizers and participants of the workshop “Universe in a box”, Lorentz Center, Leiden, NL, August 2009, where some results contained in this paper were firstly presented and discussed. A.P. thanks

the groups at CERN, Columbia U., Maryland U., Colorado U., Washington U., LLNL, SLAC, Syracuse U. for warmly hosting him and for useful and stimulating discussions about several aspects of this work. Our work has been partially supported by STFC under contracts PP/E007228/1, ST/G000506/1. B.L. is supported by the Royal Society, A.P. is supported by STFC. A.R. thanks the Deutsche Forschungsgemeinschaft for financial support.

### Appendix A: Effective mass definition

For the definition of the effective mass used in this work we follow Ref. [71]. A mesonic correlator on the lattice has the form:

$$C(\tau) = \sum_{m=1}^M a_m \cosh[E_m \tau] \quad , \quad (\text{A1})$$

with  $\tau = t - T/2 = 0, 1, 2, \dots, T/2$ , where we consider only  $M$  excited states. Now since:

$$(\cosh[E_m])^n = \frac{1}{2^n} \sum_{k=0}^n \binom{n}{k} \cosh[E_m(2k - n)] \quad , \quad (\text{A2})$$

taking similar linear combinations of the  $C(\tau)$  we have:

$$\frac{1}{2^n} \sum_{k=0}^n \binom{n}{k} C(2k - n) = \sum_{m=1}^M a_m (\cosh[E_m])^n \quad . \quad (\text{A3})$$

Introducing the variables:

$$x_m \equiv \cosh[E_m] \quad , \quad (\text{A4})$$

$$y_n \equiv \frac{1}{2^n} \sum_{k=0}^n \binom{n}{k} C(2k - n) \quad , \quad (\text{A5})$$

we can rewrite Eq. A3 in matrix form as:

$$\begin{pmatrix} y_0 \\ y_1 \\ \vdots \end{pmatrix} = \begin{pmatrix} 1 & 1 & 1 & 1 & \cdots \\ x_1 & x_2 & x_3 & x_4 & \cdots \\ x_1^2 & x_2^2 & x_3^2 & x_4^2 & \cdots \\ x_1^3 & x_2^3 & x_3^3 & x_4^3 & \cdots \\ \vdots & \vdots & \vdots & \vdots & \ddots \end{pmatrix} \cdot \begin{pmatrix} a_1 \\ a_2 \\ \vdots \end{pmatrix} \quad . \quad (\text{A6})$$

We need to solve Eq. A6 where  $y_n$  is known and both  $a_m$  and  $x_m$  are unknown. It is always possible to find the unique solution to Eq. A6 considering  $2M$  consecutive points in the transformed correlator  $y_n$ . In general the  $x_n$  are given by the roots of the  $M$ -degree polynomial:

$$\det \begin{pmatrix} y_0 & y_1 & \cdots & y_{M-1} & 1 \\ y_1 & y_2 & \cdots & y_M & x \\ y_2 & y_3 & \cdots & y_{M+1} & x^2 \\ \vdots & \vdots & & \vdots & \vdots \\ y_M & y_{M+1} & \cdots & y_{2M-1} & x^M \end{pmatrix} = 0 \quad , \quad (\text{A7})$$

and the  $a_m$  are then given by the solution of the linear system Eq.(4) obtained with the known  $x_n$ .

In this work we do not consider excited states and we only need the solution of Eq. A7 for  $M = 1$  which is given by  $x = y_1/y_0$ .

## Appendix B: Tables

- 
- [1] S. Weinberg, Phys. Rev. **D13**, 974 (1976).
  - [2] L. Susskind, Phys. Rev. **D20**, 2619 (1979).
  - [3] M. E. Peskin and T. Takeuchi, Phys. Rev. Lett. **65**, 964 (1990).
  - [4] M. E. Peskin and T. Takeuchi, Phys. Rev. **D46**, 381 (1992).
  - [5] C. Amsler et al. (Particle Data Group), Phys. Lett. **B667**, 1 (2008).
  - [6] B. Holdom, Phys. Lett. **B150**, 301 (1985).
  - [7] K. Yamawaki, M. Bando, and K.-i. Matumoto, Phys. Rev. Lett. **56**, 1335 (1986).
  - [8] T. W. Appelquist, D. Karabali, and L. C. R. Wijewardhana, Phys. Rev. Lett. **57**, 957 (1986).
  - [9] M. A. Luty and T. Okui, JHEP **09**, 070 (2006), hep-ph/0409274.
  - [10] C. T. Hill and E. H. Simmons, Phys. Rept. **381**, 235 (2003), hep-ph/0203079.
  - [11] F. Sannino (2008), 0804.0182.
  - [12] F. Sannino (2009), 0911.0931.
  - [13] M. Piai (2010), 1004.0176.
  - [14] F. Sannino and K. Tuominen, Phys. Rev. **D71**, 051901 (2005), hep-ph/0405209.
  - [15] D. D. Dietrich and F. Sannino, Phys. Rev. **D75**, 085018 (2007), hep-ph/0611341.
  - [16] S. Catterall and F. Sannino, Phys. Rev. **D76**, 034504 (2007), 0705.1664.
  - [17] T. Appelquist, G. T. Fleming, and E. T. Neil, Phys. Rev. Lett. **100**, 171607 (2008), 0712.0609.
  - [18] L. Del Debbio, M. T. Frandsen, H. Panagopoulos, and F. Sannino, JHEP **06**, 007 (2008), 0802.0891.
  - [19] Y. Shamir, B. Svetitsky, and T. DeGrand, Phys. Rev. **D78**, 031502 (2008), 0803.1707.
  - [20] A. Deuzeman, M. P. Lombardo, and E. Pallante, Phys. Lett. **B670**, 41 (2008), 0804.2905.
  - [21] L. Del Debbio, A. Patella, and C. Pica (2008), 0805.2058.
  - [22] S. Catterall, J. Giedt, F. Sannino, and J. Schneible, JHEP **11**, 009 (2008), 0807.0792.
  - [23] B. Svetitsky, Y. Shamir, and T. DeGrand, PoS **LATTICE2008**, 062 (2008), 0809.2885.
  - [24] T. DeGrand, Y. Shamir, and B. Svetitsky, PoS **LATTICE2008**, 063 (2008), 0809.2953.
  - [25] Z. Fodor, K. Holland, J. Kuti, D. Nogradi, and C. Schroeder, PoS **LATTICE2008**, 058 (2008), 0809.4888.
  - [26] Z. Fodor, K. Holland, J. Kuti, D. Nogradi, and C. Schroeder, PoS **LATTICE2008**, 066 (2008), 0809.4890.
  - [27] A. Deuzeman, M. P. Lombardo, and E. Pallante, PoS **LATTICE2008**, 060 (2008), 0810.1719.
  - [28] A. Deuzeman, E. Pallante, M. P. Lombardo, and E. Pallante, PoS **LATTICE2008**, 056 (2008), 0810.3117.
  - [29] A. Hietanen, J. Rantaharju, K. Rummukainen, and K. Tuominen, PoS **LATTICE2008**, 065 (2008), 0810.3722.
  - [30] X.-Y. Jin and R. D. Mawhinney, PoS **LATTICE2008**, 059 (2008), 0812.0413.
  - [31] L. Del Debbio, A. Patella, and C. Pica, PoS **LATTICE2008**, 064 (2008), 0812.0570.
  - [32] T. DeGrand, Y. Shamir, and B. Svetitsky, Phys. Rev. **D79**, 034501 (2009), 0812.1427.
  - [33] G. T. Fleming, PoS **LATTICE2008**, 021 (2008), 0812.2035.
  - [34] A. J. Hietanen, J. Rantaharju, K. Rummukainen, and K. Tuominen, JHEP **05**, 025 (2009), 0812.1467.
  - [35] T. Appelquist, G. T. Fleming, and E. T. Neil, Phys. Rev. **D79**, 076010 (2009), 0901.3766.
  - [36] A. J. Hietanen, K. Rummukainen, and K. Tuominen, Phys. Rev. **D80**, 094504 (2009), 0904.0864.
  - [37] A. Deuzeman, M. P. Lombardo, and E. Pallante (2009), 0904.4662.
  - [38] Z. Fodor, K. Holland, J. Kuti, D. Nogradi, and C. Schroeder, JHEP **08**, 084 (2009), 0905.3586.
  - [39] T. DeGrand and A. Hasenfratz, Phys. Rev. **D80**, 034506 (2009), 0906.1976.
  - [40] T. DeGrand (2009), 0906.4543.
  - [41] A. Hasenfratz, Phys. Rev. **D80**, 034505 (2009), 0907.0919.
  - [42] L. Del Debbio, B. Lucini, A. Patella, C. Pica, and A. Rago, Phys. Rev. **D80**, 074507 (2009), 0907.3896.
  - [43] Z. Fodor, K. Holland, J. Kuti, D. Nogradi, and C. Schroeder, Phys. Lett. **B681**, 353 (2009), 0907.4562.
  - [44] Z. Fodor, K. Holland, J. Kuti, D. Nogradi, and C. Schroeder, JHEP **11**, 103 (2009), 0908.2466.
  - [45] T. Appelquist et al., Phys. Rev. Lett. **104**, 071601 (2010), 0910.2224.
  - [46] T. DeGrand, Phys. Rev. **D80**, 114507 (2009), 0910.3072.
  - [47] S. Catterall, J. Giedt, F. Sannino, and J. Schneible (2009), 0910.4387.
  - [48] F. Bursa, L. Del Debbio, L. Keegan, C. Pica, and T. Pickup, Phys. Rev. **D81**, 014505 (2010), 0910.4535.
  - [49] B. Lucini (2009), 0911.0020.
  - [50] E. Pallante (2009), 0912.5188.
  - [51] E. Bilgici et al., Phys. Rev. **D80**, 034507 (2009), 0902.3768.
  - [52] O. Machtey and B. Svetitsky, Phys. Rev. **D81**, 014501 (2010), 0911.0886.

- [53] G. Moraitis (2009), 0911.5111.
- [54] J. B. Kogut and D. K. Sinclair (2010), 1002.2988.
- [55] A. Hasenfratz (2010), 1004.1004.
- [56] L. Del Debbio, B. Lucini, A. Patella, C. Pica, and A. Rago (2010), in preparation.
- [57] G. 't Hooft, Nucl. Phys. **B153**, 141 (1979).
- [58] M. Luscher, Nucl. Phys. **B219**, 233 (1983).
- [59] P. van Baal and J. Koller, Ann. Phys. **174**, 299 (1987).
- [60] L. Del Debbio, L. Giusti, M. Luscher, R. Petronzio, and N. Tantalo, JHEP **02**, 011 (2006), hep-lat/0512021.
- [61] L. Del Debbio, L. Giusti, M. Luscher, R. Petronzio, and N. Tantalo, JHEP **02**, 082 (2007), hep-lat/0701009.
- [62] L. Del Debbio, B. Lucini, A. Patella, and C. Pica, JHEP **03**, 062 (2008), 0712.3036.
- [63] A. Armoni, B. Lucini, A. Patella, and C. Pica, Phys. Rev. **D78**, 045019 (2008), 0804.4501.
- [64] S. Duane, A. D. Kennedy, B. J. Pendleton, and D. Roweth, Phys. Lett. **B195**, 216 (1987).
- [65] A. D. Kennedy, I. Horvath, and S. Sint, Nucl. Phys. Proc. Suppl. **73**, 834 (1999), hep-lat/9809092.
- [66] M. A. Clark and A. D. Kennedy, Nucl. Phys. Proc. Suppl. **129**, 850 (2004), hep-lat/0309084.
- [67] M. Luscher, Comput. Phys. Commun. **165**, 199 (2005), hep-lat/0409106.
- [68] P. A. Boyle, A. Juttner, C. Kelly, and R. D. Kenway, JHEP **08**, 086 (2008), 0804.1501.
- [69] D. Weingarten, Phys. Rev. Lett. **51**, 1830 (1983).
- [70] L. Giusti, F. Rapuano, M. Talevi, and A. Vladikas, Nucl. Phys. **B538**, 249 (1999), hep-lat/9807014.
- [71] G. T. Fleming, S. D. Cohen, H.-W. Lin, and V. Pereyra, Phys. Rev. **D80**, 074506 (2009), 0903.2314.

lattice	V	$-am_0$	$N_{traj}$	$\langle P \rangle$	$\tau$	$\lambda$	$\tau_\lambda$
A0	$16 \times 8^3$	0.95	7601	0.63577(16)	5.45(72)	3.582(13)	8.6(1.4)
A1	$16 \times 8^3$	0.975	7701	0.63843(15)	5.43(71)	2.982(12)	6.65(96)
A2	$16 \times 8^3$	1	7801	0.64136(15)	5.10(64)	2.427(11)	6.28(88)
A3	$16 \times 8^3$	1.025	7801	0.64463(15)	4.29(50)	1.894(10)	6.07(84)
A4	$16 \times 8^3$	1.05	7801	0.64793(15)	3.48(36)	1.4596(79)	4.39(52)
A5	$16 \times 8^3$	1.075	6400	0.65179(16)	2.99(32)	1.0692(74)	4.27(55)
A6	$16 \times 8^3$	1.1	6400	0.65566(16)	3.28(37)	0.7564(60)	3.77(45)
A7	$16 \times 8^3$	1.125	7073	0.66037(15)	2.99(30)	0.4854(43)	3.03(31)
A8	$16 \times 8^3$	1.15	6400	0.66550(16)	3.31(37)	0.2779(31)	2.80(29)
A9	$16 \times 8^3$	1.175	6400	0.67177(17)	3.24(36)	0.1351(18)	2.80(29)

TABLE I: Bare parameters and average plaquette for the  $16 \times 8^3$  lattice.

lattice	$-am_0$	$am$	$aM_{PS}$	$aM_V$	$aF_{PS}$	$a^2 G_{PS}$
A0	0.95	0.3899(40)	1.4717(40)	1.5203(52)	0.3354(60)	0.933(13)
A1	0.975	0.3649(41)	1.4093(43)	1.4586(55)	0.3240(61)	0.883(13)
A2	1	0.3365(42)	1.3436(43)	1.3936(58)	0.3083(62)	0.829(13)
A3	1.025	0.3066(38)	1.2630(46)	1.3115(59)	0.2908(58)	0.759(12)
A4	1.05	0.2749(39)	1.1756(48)	1.2233(64)	0.2666(58)	0.673(11)
A5	1.075	0.2389(39)	1.0623(56)	1.1048(72)	0.2392(59)	0.567(11)
A6	1.1	0.2031(39)	0.9398(66)	0.9784(86)	0.2157(59)	0.472(11)
A7	1.125	0.1643(36)	0.7817(76)	0.811(10)	0.1910(57)	0.357(10)
A8	1.15	0.1185(32)	0.5740(89)	0.587(11)	0.1675(56)	0.2347(82)
A9	1.175	0.0650(24)	0.330(11)	0.3476(91)	0.1611(50)	0.1347(76)

TABLE II: PCAC and meson masses from the  $16 \times 8^3$  lattice.

lattice	$-am_0$	$am$	$aM_{PS}^2/m$	$M_V/F_{PS}$	$M_V/M_{PS}$	$a^3(M_{PS}F_{PS})^2/m$
A0	0.95	0.3899(40)	5.554(62)	4.533(77)	1.0330(12)	0.625(19)
A1	0.975	0.3649(41)	5.443(67)	4.502(79)	1.0349(13)	0.571(18)
A2	1	0.3365(42)	5.365(71)	4.521(86)	1.0372(15)	0.510(17)
A3	1.025	0.3066(38)	5.203(70)	4.511(84)	1.0384(17)	0.440(15)
A4	1.05	0.2749(39)	5.027(77)	4.589(94)	1.0405(22)	0.357(13)
A5	1.075	0.2389(39)	4.724(83)	4.62(10)	1.0399(28)	0.270(11)
A6	1.1	0.2031(39)	4.349(92)	4.53(11)	1.0410(37)	0.2025(96)
A7	1.125	0.1643(36)	3.721(92)	4.24(11)	1.0375(53)	0.1358(74)
A8	1.15	0.1185(32)	2.782(90)	3.51(11)	1.0242(88)	0.0781(48)
A9	1.175	0.0650(24)	1.67(10)	2.159(80)	1.054(31)	0.0434(30)

TABLE III: Mass ratios from the  $16 \times 8^3$  lattice.

lattice	V	$-am_0$	$N_{traj}$	$\langle P \rangle$	$\tau$	$\lambda$	$\tau_\lambda$
B0	$24 \times 12^3$	0.95	10201	0.635310(59)	6.16(74)	3.5058(50)	3.08(26)
B1	$24 \times 12^3$	1	8652	0.640998(64)	4.92(58)	2.4218(44)	3.10(29)
B2	$24 \times 12^3$	1.05	7819	0.647633(70)	6.79(99)	1.4936(51)	5.80(78)
B3	$24 \times 12^3$	1.075	7186	0.651630(68)	4.61(58)	1.0553(40)	4.95(64)
B4	$24 \times 12^3$	1.1	6393	0.655827(76)	4.09(51)	0.7202(30)	7.8(1.3)
B5	$24 \times 12^3$	1.125	6200	0.660588(75)	3.97(50)	0.4419(22)	5.98(91)
B6	$24 \times 12^3$	1.15	1599	0.66588(15)	3.71(90)	0.2271(31)	6.6(2.1)
B7	$24 \times 12^3$	1.175	5582	0.672074(79)	4.22(58)	0.08641(90)	3.78(49)
B8	$24 \times 12^3$	1.18	4081	0.673474(92)	4.01(63)	0.06561(92)	10(2.5)
B9	$24 \times 12^3$	1.185	4201	0.675094(93)	3.42(49)	0.05196(71)	3.53(51)
B10	$24 \times 12^3$	1.19	3501	0.67663(10)	4.15(70)	0.03985(61)	5.2(1.0)

TABLE IV: Bare parameters and average plaquette for the  $24 \times 12^3$  lattice.

lattice	$-am_0$	$am$	$aM_{PS}$	$aM_V$	$aF_{PS}$	$a^2G_{PS}$
B0	0.95	0.3931(38)	1.4746(23)	1.5224(32)	0.3343(62)	0.925(12)
B1	1	0.3368(40)	1.3495(26)	1.4003(36)	0.3020(63)	0.819(12)
B2	1.05	0.2765(40)	1.1874(29)	1.2383(40)	0.2607(63)	0.667(11)
B3	1.075	0.2410(38)	1.0809(30)	1.1265(41)	0.2320(58)	0.5635(96)
B4	1.1	0.2025(40)	0.9614(35)	1.0016(46)	0.1991(53)	0.4558(85)
B5	1.125	0.1604(34)	0.8020(41)	0.8312(56)	0.1628(49)	0.3277(71)
B6	1.15	0.1198(52)	0.6111(91)	0.627(11)	0.1313(78)	0.2066(97)
B7	1.175	0.0660(22)	0.3593(52)	0.3659(66)	0.1083(40)	0.1055(33)
B8	1.18	0.0565(23)	0.3085(60)	0.3199(76)	0.1108(47)	0.0927(35)
B9	1.185	0.0430(18)	0.2292(69)	0.2277(85)	0.1090(44)	0.0664(32)
B10	1.19	0.0302(16)	0.1664(81)	0.165(10)	0.1083(45)	0.0506(34)

TABLE V: PCAC and meson masses from the  $24 \times 12^3$  lattice.

lattice	$-am_0$	$am$	$aM_{PS}^2/m$	$M_V/F_{PS}$	$M_V/M_{PS}$	$a^3(M_{PS}F_{PS})^2/m$
B0	0.95	0.3931(38)	5.531(55)	4.555(81)	1.03241(85)	0.618(19)
B1	1	0.3368(40)	5.406(67)	4.637(93)	1.0376(11)	0.493(17)
B2	1.05	0.2765(40)	5.098(77)	4.75(11)	1.0428(14)	0.346(13)
B3	1.075	0.2410(38)	4.849(78)	4.85(11)	1.0421(16)	0.261(10)
B4	1.1	0.2025(40)	4.564(93)	5.03(12)	1.0418(20)	0.1810(75)
B5	1.125	0.1604(34)	4.010(90)	5.10(14)	1.0364(30)	0.1063(51)
B6	1.15	0.1198(52)	3.12(15)	4.79(27)	1.0272(80)	0.0539(53)
B7	1.175	0.0660(22)	1.958(74)	3.38(12)	1.0183(86)	0.0229(13)
B8	1.18	0.0565(23)	1.687(81)	2.89(13)	1.036(13)	0.0207(13)
B9	1.185	0.0430(18)	1.223(73)	2.09(11)	0.993(18)	0.0145(10)
B10	1.19	0.0302(16)	0.918(85)	1.53(11)	0.996(39)	0.01076(98)

TABLE VI: Mass ratios from the  $24 \times 12^3$  lattice.

lattice	V	$-am_0$	$N_{traj}$	$\langle P \rangle$	$\tau$	$\lambda$	$\tau_\lambda$
C0	$32 \times 16^3$	1.15	5446	0.665894(44)	3.32(40)	0.2227(10)	3.05(36)
C1	$32 \times 16^3$	1.175	2192	0.672235(73)	2.80(50)	0.07036(90)	5.9(1.5)
C2	$32 \times 16^3$	1.18	4606	0.673657(49)	3.46(47)	0.05167(50)	6.1(1.1)
C3	$32 \times 16^3$	1.185	4313	0.675170(50)	2.99(39)	0.03751(38)	4.66(75)
C4	$32 \times 16^3$	1.19	5404	0.676637(44)	3.29(40)	0.02474(28)	7.9(1.5)

TABLE VII: Bare parameters and average plaquette for the  $32 \times 16^3$  lattice.

lattice	$-am_0$	$am$	$aM_{PS}$	$aM_V$	$aF_{PS}$	$a^2G_{PS}$
C0	1.15	0.1175(30)	0.6319(31)	0.6541(43)	0.1196(41)	0.2037(49)
C1	1.175	0.0678(30)	0.3834(49)	0.4015(61)	0.0919(51)	0.1018(37)
C2	1.18	0.0549(18)	0.3226(37)	0.3364(46)	0.0860(35)	0.0817(24)
C3	1.185	0.0420(16)	0.2416(39)	0.2443(50)	0.0784(32)	0.0542(18)
C4	1.19	0.0308(10)	0.1842(36)	0.1900(43)	0.0806(29)	0.0443(15)

TABLE VIII: PCAC and meson masses from the  $32 \times 16^3$  lattice.

lattice	$-am_0$	$am$	$aM_{PS}^2/m$	$M_V/F_{PS}$	$M_V/M_{PS}$	$a^3(M_{PS}F_{PS})^2/m$
C0	1.15	0.1175(30)	3.398(90)	5.47(18)	1.0351(35)	0.0486(26)
C1	1.175	0.0678(30)	2.17(10)	4.38(23)	1.0473(93)	0.0183(15)
C2	1.18	0.0549(18)	1.895(70)	3.91(16)	1.0426(86)	0.01404(89)
C3	1.185	0.0420(16)	1.390(61)	3.12(13)	1.011(12)	0.00854(52)
C4	1.19	0.0308(10)	1.102(53)	2.36(10)	1.031(18)	0.00715(38)

TABLE IX: Mass ratios from the  $32 \times 16^3$  lattice.

lattice	V	$-am_0$	$N_{traj}$	$\langle P \rangle$	$\tau$	$\lambda$	$\tau_\lambda$
D0	$64 \times 24^3$	1.18	458	0.673737(46)	4.0(1.9)	0.04436(51)	3.5(1.5)
D1	$64 \times 24^3$	1.185	291	0.675184(59)	2.3(1.1)	0.02836(59)	4.2(2.5)
D2	$64 \times 24^3$	1.19	349	0.676649(52)	1.63(59)	0.01520(39)	5.7(3.6)

TABLE X: Bare parameters and average plaquette for the  $64 \times 24^3$  lattice.

lattice	$-am_0$	$am$	$aM_{PS}$	$aM_V$	$aF_{PS}$	$a^2G_{PS}$
D0	1.18	0.0562(25)	0.3433(37)	0.3597(56)	0.0620(42)	0.0661(31)
D1	1.185	0.0445(36)	0.2930(73)	0.325(11)	0.0629(53)	0.0580(52)
D2	1.19	0.0330(25)	0.2184(73)	0.230(10)	0.0534(50)	0.0388(38)

TABLE XI: PCAC and meson masses from the  $64 \times 24^3$  lattice.

lattice	$-am_0$	$am$	$aM_{PS}^2/m$	$M_V/F_{PS}$	$M_V/M_{PS}$	$a^3(M_{PS}F_{PS})^2/m$
D0	1.18	0.0562(25)	2.099(97)	5.82(37)	1.0477(98)	0.00808(93)
D1	1.185	0.0445(36)	1.94(19)	5.20(46)	1.110(22)	0.00768(99)
D2	1.19	0.0330(25)	1.45(13)	4.34(40)	1.054(24)	0.00415(73)

TABLE XII: Mass ratios from the  $64 \times 24^3$  lattice.